

Breaking down chipping and fragmentation in sediment transport: the control of material strength

Sophie Bodek¹ and Douglas J. Jerolmack^{2,3}

¹Department of Earth Sciences, University of Delaware, Newark, Delaware, USA

²Department of Earth and Environmental Science, University of Pennsylvania, Philadelphia, Pennsylvania, USA

³Mechanical Engineering and Applied Mechanics, University of Pennsylvania, Philadelphia, Pennsylvania, USA

Correspondence: sbodek@udel.edu

Abstract. As rocks are transported, they primarily undergo two breakdown mechanisms: chipping and fragmentation. Chipping occurs at relatively low collision energies typical of bed-load transport, and involves shallow cracking; this process rounds river pebbles in a universal manner. Fragmentation involves catastrophic breakup by fracture growth in the bulk — a response that occurs at high collision energies such as rock falls — and produces angular shards. Despite its geophysical significance, the transition from chipping to fragmentation is not well studied. Here we experimentally delineate the boundary between chipping and fragmentation by examining the mass and shape evolution of concrete particles in a rotating drum. Attrition rate should be a function of both impact energy and material strength; here we keep the former roughly constant, while systematically varying the latter. For sufficiently strong particles, chipping occurred and was characterized by the following: attrition products were significantly smaller than the parent; attrition rate was insensitive to material strength; and particles experienced monotonic rounding toward a spherical shape. As strength decreased, fragmentation became more significant: mass of attrition products became larger and more varied; attrition rate was inversely proportional to material strength; and shape evolution fluctuated and became non-monotonic. Our results validate conceptual and numerical models for impact attrition, and indicate that bedrock erosion models must be clarified to incorporate distinct attrition mechanisms. We suggest that the shape of natural pebbles may be utilized to deduce the breakdown mechanism, and infer past transport environments.

1 Introduction

The energy associated with transporting sediment influences the shape of the particles being moved. Events such as rock falls, landslides, or debris flows tend to be highly energetic and cause rocks to fragment into large, angular pieces (Bernd et al., 2010; Arabnia and Sklar, 2016). Bed-load transport is of lower energy, and causes river rocks to round into smooth pebbles (Krumbein, 1941; Kuenen, 1956; Attal and Lavé, 2009; Domokos et al., 2014). The attrition mechanism that occurs during transport depends on impact energy and material properties, including size, shape, and material strength (Yashima et al., 1987; Tavares and King, 1998; Sklar and Dietrich, 2004; Salman et al., 2004a; Tavares and das Neves, 2008; Domokos et al., 2015; Pal et al., 2021); these attrition mechanisms have been classified using the terms *frictional abrasion*, *chipping*, and *fragmentation* (Bemrose and Bridgwater, 1987; Ghadiri and Zhang, 2002). Our study examines the chipping and fragmentation regimes, and how material strength influences attrition mechanism (Fig. 1).

It is common to cast the impact attrition process in terms of the mass lost per collision, Δm . This mass loss is presumed to be proportional to collision energy, ΔE , such that:

$$\Delta m = C_1 A_b \Delta E \quad (1)$$

where A_b is a material susceptibility parameter (Anderson, 1986) that Miller and Jerolmack (2020) called the “Brittle Attrition Number” [$s^2 \text{ m}^{-2}$], and C_1 is an experimentally determined constant (following the nomenclature of Miller and Jerolmack (2020)). Since collision energy is a function of the mass of the particle, m , and impact velocity, v_i , where $\Delta E = \frac{1}{2} m v_i^2$, this relation implies Sternberg’s law (Sternberg, 1875) — i.e., that mass should decrease exponentially with number of impacts (or, similarly, transport distance) (Novák-Szabó et al., 2018). It has been proposed that susceptibility to fracture in brittle materials depends on a material’s ability to store energy elastically (Engle, 1978; Wang et al., 2011). From mechanical considerations and dimensional analysis, several studies have arrived at a similar parameter (Sklar and Dietrich, 2004; Wang et al., 2011; Miller and Jerolmack, 2020):

$$A_b = \frac{\rho_s Y}{\sigma_s^2}, \quad (2)$$

where σ_s is yield strength [N m^{-2}], Y is Young’s modulus [N m^{-2}], and ρ_s is the density of the material [kg m^{-3}]. The parameter A_b was found to reasonably describe the control of material properties on the attrition rate of natural rocks undergoing low-energy collisions (Miller and Jerolmack, 2020). For this reason, we will use A_b to characterize material strength in our study.

The characteristic smooth, round shape of pebbles is the result of chipping, when low-energy collisions cause small particles to break off the parent rock (Rogers and Schubert, 1963; Ghadiri and Zhang, 2002; Jerolmack and Brzinski, 2010; Pal et al., 2021). Lateral cracking is known to produce chipping in natural rock materials (Wilshaw, 1971). A recent experimental study on binary collisions of rocks (Miller and Jerolmack, 2020), with energies representative of bed-load transport, showed that chipping involves fragmentation within a shallow region that is bounded from below by surface-parallel cracks (Fig. 2). At the contact zones of low-velocity impacts, compression crack cones generically form for a wide range of materials (Salman et al., 2004a). In brittle glasses and ceramics, this mode of cracking corresponds to Hertzian fracture (Wilshaw, 1971; Greeley and Iversen, 1987; Mohajerani and Spelt, 2010; Wang et al., 2017). For sufficiently brittle materials (including rocks and many building materials), plastic deformation and yielding in a localized region generally occurs on unloading of the compressive impact stress (Rhee et al., 2001; Ghadiri and Zhang, 2002; Wilshaw, 1971; Salman et al., 2004a); in collisions, this corresponds to rebound.

In the chipping regime of impact attrition, each collision produces a shower of fine particles that are orders of magnitude smaller than the parent (Miller and Jerolmack, 2020; Pal et al., 2021). In this limit, the shape evolution of both natural and artificial pebbles can be modeled purely geometrically. Essentially, areas that protrude from the pebble have a positive curvature and are more likely to strike another particle or the bed surface, and chip off. Thus, particles undergo curvature-driven attrition that initially evolves their shape toward a sphere (Firey, 1974; Domokos et al., 2009; Várkonyi and Domokos, 2011; Domokos et al., 2014). In the typical case of bed load with gravels impacting a streambed, it has been found that initially angular river

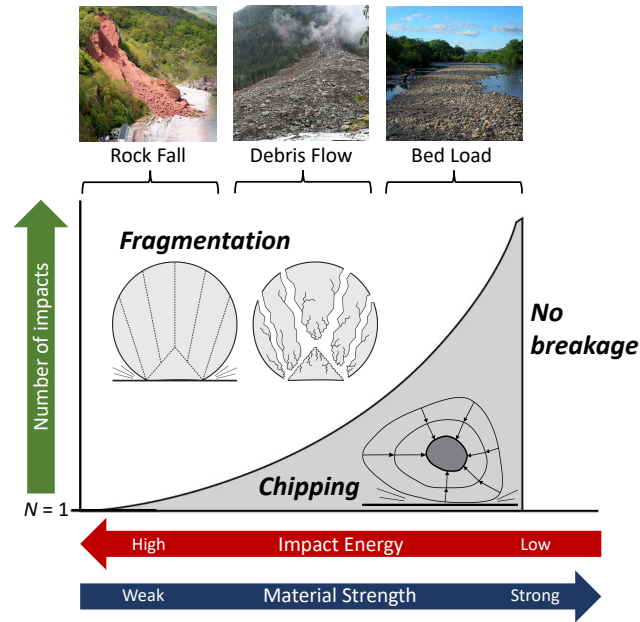


Figure 1. Schematic phase diagram delineating the attrition mechanism as a function of impact energy (influenced by collision velocity and particle mass) or material strength, and number of impacts; adapted from the proposed diagram of Zhang and Ghadiri (2002). For extremely weak materials or high impact energies (left), explosive fragmentation can occur from a single collision. As material strength increases or impact energy decreases (center), fragmentation occurs through fatigue failure, where cracks grow progressively through the material with each collision. In the limit of pure chipping, which applies to low impact energies or strong materials (right), the number of impacts required to produce fragmentation increases toward infinity. Examples of transport mechanisms associated with fragmentation, fatigue failure, and pure chipping are rock falls, debris flows, and bed-load transport, respectively. Fragmentation figure is adapted from Salman et al. (2004b); chipping figure is adapted from Szabó et al. (2013); photographs of transport mechanisms are reproduced from Wikimedia Commons.

pebbles round in a universal manner. While in situ weathering has been observed to produce rounded clasts in a wide variety of rock types (e.g., Chapman and Greenfield, 1949; Simpson, 1964; Ollier, 1967; Okumura, 1982; Sak et al., 2010), sediments delivered to steep headwater regions tend to be fragmented through landslides or debris flows (e.g., Beschta, 1983; van Steijn, 1996; Hovius et al., 1997, 2000). Thus, the shape change from angular to smooth can be attributed to attrition and is the signature of the chipping process (Szabó et al., 2013; Miller et al., 2014; Szabó et al., 2015; Novák-Szabó et al., 2018). This universality has been used to infer the transport distance of river pebbles from measurements of their shape (e.g., Szabó et al., 2013, 2015).

Unlike chipping, catastrophic fragmentation occurs when high-energy collisions cause cracks to propagate radially into the bulk. These radial cracks can split the parent rock into irregularly-shaped attrition products whose size is a significant fraction of the parent, in addition to smaller fragments (Moss et al., 1973; Adams, 1979; Bernd et al., 2010; Arabnia and Sklar, 2016; Perfect, 1997; Kun and Herrmann, 1999; Salman et al., 2004b; Grady, 2010). The mass and shape distributions of

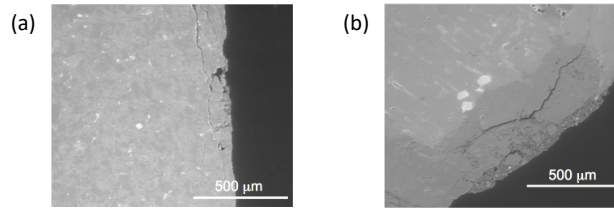


Figure 2. Scanning electron microscope images depicting subsurface lateral cracks, formed after repeated binary collisions of rocks at energies representative of bed-load transport. We speculate that these cracks, and the shattered region bounded by them, are the result of compressive fracture cones formed by impulsive collisions. Images show thin sections of (a) quartz diorite, and (b) volcanoclastic rock. Figure reproduced from Miller and Jerolmack (2020).

particles formed by fragmentation have their own universal characteristics (Domokos et al., 2015, 2020) that make them easily distinguishable from particles undergoing chipping.

While the low and high energy limits of attrition — corresponding respectively to chipping and fragmentation — are well established, the transition from one regime to the other is much less studied. At intermediate impact energies, fatigue failure may occur as fractures gradually grow into the rock as a result of repeated impacts (Bitter, 1963; Moss et al., 1973; Salman et al., 2004a; Pal et al., 2021). Ghadiri and Zhang (2002) proposed a conceptual model that envisioned the transition from chipping to fragmentation as a continuous phase transition, and as a function of impact energy. A remarkable recent study, that simulated impact attrition with the high-fidelity discrete element method (DEM), found and quantified this continuous phase transition (Pal et al., 2021). In the low-energy limit of chipping, these simulations reproduced both Sternberg’s law (Sternberg, 1875; Kodama, 1994; Lewin and Brewer, 2002; Novák-Szabó et al., 2018) and the universal rounding pattern associated with bed load (Szabó et al., 2015; Novák-Szabó et al., 2018). Model runs established a range of impact energies under which chipping occurred, and the average size of attrition products grew slowly with increasing impact energy (Pal et al., 2021). Beyond a critical energy, they found a damage regime (which they termed ‘cleavage’) that corresponded to fatigue failure. The average size of attrition products grew rapidly with collision energy, with large fragments resulting from progressive crack growth over several collisions. In this intermediate regime, particle shape evolution became more erratic and departed from the universal chipping trend (Pal et al., 2021). Finally, for sufficiently large energies they observed explosive fragmentation, in which the size of attrition products actually declined because the particles were pulverized.

Determining the mechanism of impact attrition in nature is relevant not only for inferring transport conditions of pebbles, but also for modeling fluvial bedrock erosion due to bed-load transport. For the latter, it is likely that both chipping and fatigue failure are relevant attrition mechanisms, depending on rock properties and collision energy. Yet, existing “saltation abrasion” models do not distinguish among them (Sklar and Dietrich, 2001, 2004). The Pal et al. (2021) simulation results provide new insight on the nature of the transition from chipping to fragmentation, and the signatures of each process encoded in shape and mass loss trends. However, their results have not yet been confirmed with laboratory experiments. Moreover, while models for impact attrition indicate that both energy and material properties determine mass loss (Eq. 1), most studies of single-

impact mechanics focus on collision energy (Salman et al., 2004a; Pal et al., 2021). On the other hand, studies of bedrock and pebble erosion by “saltation abrasion” (Sklar and Dietrich, 2001, 2004; Attal and Lavé, 2009) have varied both energy and material strength; however, their complex experimental settings, meant to better simulate natural bed-load transport, preclude isolating the control of these variables on attrition mechanics. The main purpose of our paper here is to provide the first experimental validation of a continuous phase transition from chipping to fragmentation. A secondary goal is to demonstrate that this transition can be forced by changes in material strength, and to examine impact energies and material strengths that are relevant for sediment particles in nature. We perform laboratory experiments in which artificial particles with varying strength are repeatedly dropped in a rotating drum. The nature of the collisions is intentionally simplified; idealized particles created from cement-sand mixtures are utilized in order to isolate and tune material control, thus determining its influence on attrition mechanics. By measuring attrition rate, particle shape, and material strength under a known collision energy, we are able to characterize the relevant quantities needed to examine the transition from chipping to fragmentation.

2 Methods

Experiments were conducted by placing concrete blocks of varying strength in a rotating drum. The use of concrete as a synthetic, brittle rock is common in experiments of fluvial bedrock erosion, and its mechanical behavior compares well to natural rocks (e.g., Sklar and Dietrich, 2001; Johnson and Whipple, 2007). The concrete blocks were created by pouring a mixture of concrete mix (Quikrete product no. 1101) and coarse sand into 6-cm cubical molds (Fig. 3a). While concrete mixes meant for general construction purposes usually consist of gravel, sand, and Portland cement, the concrete mix used in the experiments was sieved to remove all clasts larger than coarse sand. The ratio of concrete mix to sand was varied in order to create particles of different strength with varying material susceptibility parameters (A_b) that would undergo chipping, fragmentation, or a combination of the two breakdown mechanisms in the rotating drum. A total of 10 different mixtures were created — 80 %, 75 %, 66.7 %, 50 %, 33.3 %, 25 %, 20 %, 16.7 %, 14.3 %, and 12.5 % — where percentage indicates volume of concrete mix in the mixture (VCM). There were 5 particles created for each mixture, resulting in a total of 50 concrete particles tested. For all sand and concrete mixtures, water was added for an approximately 0.4–0.6 water-to-sand/cement mixture ratio. Efforts were taken to ensure that the sand and cement mix were uniformly combined before water was added. Particles were left to cure for 10 to 15 days before being used in experiments.

Once the concrete particles had dried, each particle was individually placed in a 208.2 L (55 gal.) open head carbon steel drum with a lid fastened by a bolt ring closure (Fig. 3b). The drum was 57.15 cm in diameter and 83.31 cm long; all experiments were run with the drum rotating in the counterclockwise direction at 20 rotations per minute. A steel paddle was attached to the interior of the drum to ensure that the particle would collide with the side of the drum, as opposed to sliding along the bottom during the experiment. It was assumed that the particle impacted the side of the drum once per rotation; impact velocity was estimated to be 3.35 m s^{-1} . Each particle was rotated in specific intervals — and thus experienced a certain number of impacts — in accordance with its composition. Weaker particles (12.5–20 % VCM) were removed after every impact and were significantly diminished at the conclusion of experiments, intermediate particles (25–50 % VCM) were rotated in intervals

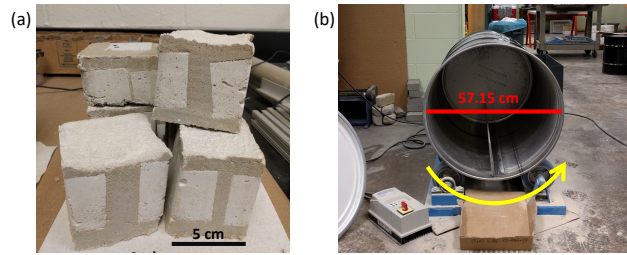


Figure 3. Experimental materials and setup. (a) Concrete particles prior to breakdown in the drum. (b) The 208.20 L (55 gal.) carbon steel drum used for collision experiments. The drum is 57.15 cm in diameter, 83.31 cm long, and rotates counterclockwise at 20 rotations per minute.

from 5 to 20 drops, and stronger particles (66.7-80 % VCM) remained in the drum for intervals ranging from 50 to 500 drops. After each interval, the particle was removed from the drum, weighed, and photographed before being returned to the drum to undergo another series of impacts. Camera resolution was 12.2 MP, and particles were photographed perpendicular to their initial orientation as long as the original sides were able to be distinguished.

5 At the conclusion of the rotating drum experiments, all images were analyzed using ImageJ. The image processing program converted the original photograph into a binary image in order to isolate the shape of the particle and measure shape parameters, including area, perimeter, circularity, and aspect ratio (Fig. 4). To verify the circularity measurements calculated by the image processing program, the shape measurement algorithm was applied to synthetic circles and squares of known shape. While measured circularity was found to be resolution dependent, the maximum error was 10% over the resolution range that is
10 relevant for our experiments due to pixelation inherent in even idealized synthetic shapes.

An Instron Universal Testing System (Model 2406) was utilized to conduct uniaxial compression tests of the concrete particles. The same 10 mixtures of concrete mix and sand were used as in the rounding experiments, with 5 cubic particles created from each mixture. These particles were prepared independently of those used in rounding experiments using the same protocols as outlined above; however, slight variations in water content and curing time did occur. Efforts were taken to ensure
15 that cube surfaces in contact with the Instron were smooth and parallel, although this was not always achieved. A 25 kN load cell was used for the particles made of 12.5 % to 50 % VCM, and a 150 kN load cell was used for particles with 66.7 % to 80 % VCM. During the compression tests, the upper plate was driven down at a constant rate of 3 mm min^{-1} with maximum deformation set at 6 mm.

Thus, the compression experiments produced a series of stress-strain curves, which were used to determine material prop-
20 erties of the various concrete mixtures. Yield strength — the transition from (linear) elastic behavior to plastic deformation on a stress-strain curve — is frequently used as a measure of material strength. However, our stress-strain curves were highly variable, especially for weaker materials that did not follow classic brittle failure (Fig. 5a). Accordingly, here we use ultimate strength, the greatest stress withstood by a material. This procedure is analogous to the point load test method that is often used to estimate yield stress, since the latter is proportional to ultimate strength (Perras and Diederichs, 2014). Young's Modulus is

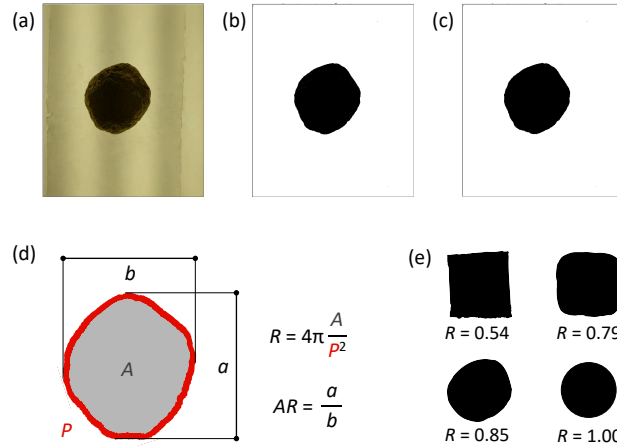


Figure 4. A visual depiction of the ImageJ macro used to determine shape parameters. First, a photograph was taken of the particle at a fixed distance over an LED light table. The macro (a) cropped the image to include only the particle, (b) converted the original image into a binary image, then (c) filled any holes within the particle shape. The macro then (d) measured the area (A), perimeter (P), major axis (a), and minor axis (b) of the particle. These measurements were used to calculate circularity (R) and aspect ratio (AR), parameters that were used to quantify shape change over the course of the rounding experiments. Circularity measures how closely a shape approaches that of a circle, where $R = 1$ indicates a perfect circle and $R < 1$ indicates deviations from a circle. Part (e) shows circularity measurements for particles of different shapes.

typically determined from a linear fit to the stress-strain plot — i.e., in the elastic regime before failure. Due to the variable shapes of our stress-strain curves, we utilized a modified Young's Modulus (Y^*), which was estimated as the ultimate strength divided by the associated strain (Fig. 5a), in order to avoid ambiguity of how to choose an approximately linear regime over which to fit.

5 3 Results

3.1 Material Properties

There was significant variation in the ultimate strengths and modified Young's Moduli recorded for each set of particles, as well as the shapes of the stress-strain curves (Fig. 5). We acknowledge that this variation is likely related to lack of control in the preparation protocol. Some of our stress-strain curves do not follow the typical linear-elastic to sub-linear plastic pattern, but instead display a series of peaks in the transition from the elastic to the plastic regime (Fig. 5a). This variation in particle strength and behavior, in response to compressional stress, is likely due to inconsistencies inherent in the process of making these concrete particles. It is possible that inhomogeneities produced during particle creation, including air bubbles, caused the curves to deviate from industrially produced concrete (e.g., Lan et al., 2010). Furthermore, molds used to create the concrete particles varied in shape from 6 cm to 8 cm, and asperities would form on the concrete along the open side of the mold. These

asperities may have influenced compression testing by reducing the ultimate strength of each particle. The compressing plates should come into contact with flat surfaces; asperities would cause the force to load unevenly and may result in premature failure and the observed peaks in the stress-strain curves (e.g., Vasconcelos and Lourenço, 2009). While these caveats make us hesitant to interpret the trends between composition and measured material properties too finely given the noise, results are generally consistent with expectations for cement.

An analysis of uniaxial compression test results revealed that particles with a higher percentage of concrete mix generally had a greater ultimate strength, σ_u (Fig. 5b). Mechanically strong particles could withstand loads ranging from 2.9×10^6 to 7.3×10^6 N m⁻², although the strongest particle (66.7 % VCM) held up to 1.2×10^7 N m⁻². Mechanically weaker particles could hold loads ranging from 9.7×10^4 to 1.2×10^6 N m⁻², although the weakest material (12.5 % VCM) withstood as little as 4.3×10^4 N m⁻² before failing (Fig. 5b). For cement mixtures, it is commonly observed that strength increases with increasing concrete content until a maximum is reached, beyond which strength drops because sand/aggregate grains lose contact with each other and no longer bear the load (Lan et al., 2010). Our results are consistent with this behavior. A similar trend was observed in particles' resistance to deformation, as measured through the modified Young's Modulus parameter, Y^* . Mechanically strong particles had modified Young's Moduli ranging from 4.3×10^7 to 1.6×10^8 N m⁻², although the strongest particle (66.7 % VCM) had a modified Young's Modulus measured at 3.8×10^8 N m⁻². Mechanically weaker particles had modified Young's Moduli ranging from 1.5×10^6 to 1.1×10^7 N m⁻², although the weakest material (12.5 % VCM) had a modified Young's Modulus measured at 2.7×10^5 N m⁻² (Fig. 5c).

The density of each type of concrete particle was also calculated from measured weight and volume for each cube estimated from axis dimensions of the molds. Density did not vary systematically with material strength; however, the average density was approximately $\rho_s = 2000$ kg m⁻³, with a range of approximately ± 35 %. This variation in density is significant, and again is likely related to lack of control in the sample preparation procedure. The brittle attrition number, A_b , was calculated using the measured values of ultimate strength, modified Young's Modulus, and density for each particle (Eq. 2). Brittle attrition number values ranged from 1.3×10^{-2} to 6.6×10^{-3} s² m⁻² for mechanically strong materials. Despite variability in the data, a clear trend is apparent between A_b and composition; A_b drops rapidly with increasing cement content, and appears to reach a roughly constant value for cement contents of 50 % VCM or greater (Fig. 5d). Results show that our samples span an order of magnitude of susceptibility to impact, as quantified by A_b , and thus that there is a significant dynamic range for exploring the control of material properties on attrition mechanism and rates. For the rest of the manuscript, we use A_b to represent material properties, and terms such as 'strong' and 'weak' refer to relatively small and large values of A_b , respectively. The average measured values of σ_u and Y^* , as well as the average calculated values of A_b , for each particle composition are reported in Figure 9.

3.2 Mass Loss

The mass of each particle decreased as that particle rotated in the metal drum. To quantify and characterize mass loss, we utilize the following parameters: mass fraction (M), cumulative mass loss (μ), and fractional mass loss per impact (Δm_*). Mass fraction is defined as the ratio of the mass of the particle during a given rotation to the initial particle mass ($M = m_i/m_o$).

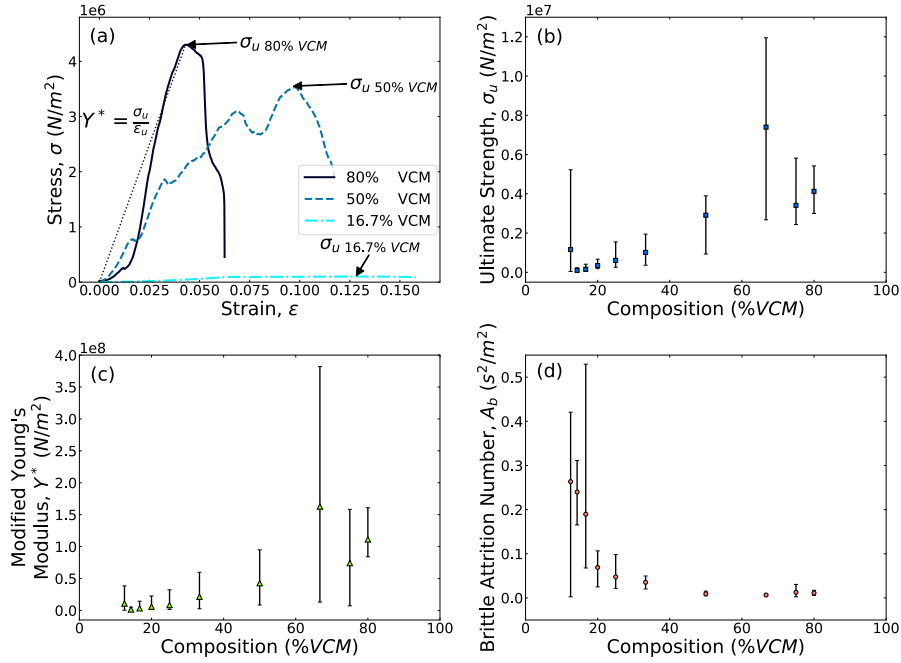


Figure 5. Material strength properties determined by uniaxial compression tests. (a) Stress-strain curves for concrete particles with varying proportions of concrete mix. Ultimate strength, σ_u [N m⁻²], is defined as the greatest stress withstood by the particle and is indicated on the stress-strain figure. Modified Young's Modulus, Y^* [N m⁻²], is calculated as the ultimate strength divided by the corresponding strain ($Y^* = \sigma_u/\epsilon_u$). (b) Average ultimate strength for each particle composition, where error bars indicate the range of values produced by experiments ($n = 5$). (c) Average modified Young's Modulus for each particle composition, where error bars indicate the range of values produced by experiments ($n = 5$). (d) Average brittle attrition number, A_b [s² m⁻²], for each particle composition, where error bars indicate the range of values produced by experiments ($n = 5$).

Cumulative mass loss is the ratio of remaining mass to the initial particle mass ($\mu = 1 - M$). Fractional mass loss per impact is the ratio of the mass lost during a given impact to the particle mass just prior to that impact ($\Delta m_* = (m_{i-1} - m_i)/m_{i-1} = \Delta m/m_{i-1}$).

Mass fraction for all particles generally decreased exponentially with impact number — i.e., data followed Sternberg's law (Fig. 6a, c, e). For strong particles (small A_b), this exponential decay was smooth and repeatable. Moreover, fractional mass loss per impact remained very small, with approximately constant (Fig. 6b, d, f) averages and little variability (Fig. 7). In other words, strong materials exhibited attrition behavior consistent with chipping. As strength decreased (A_b increased), mass loss became more erratic (Fig. 6) and the fractional mass loss per impact became increasingly large and variable (Fig. 6b, d, f; Fig. 7). The weakest particles sustained the greatest fluctuations in mass loss, indicating that these particles experienced multiple fragmentation events as they rotated in the drum.

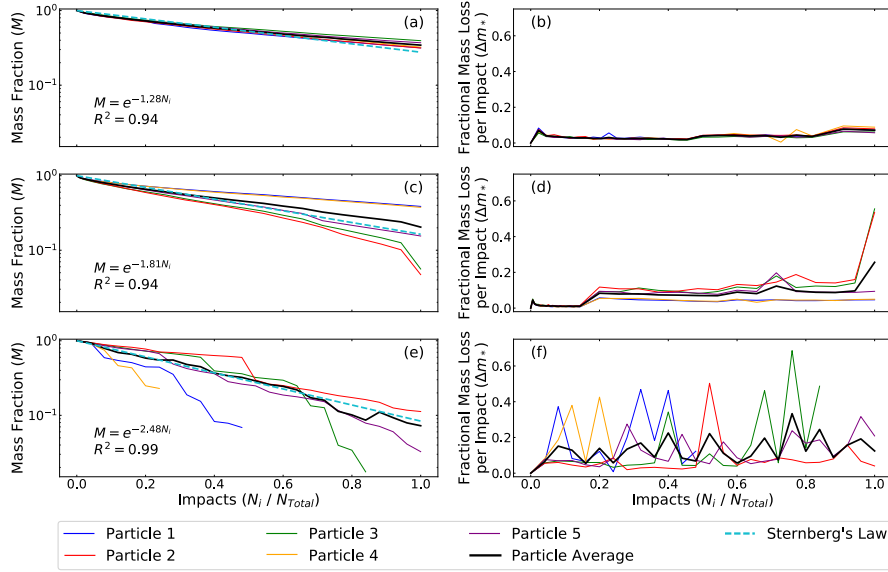


Figure 6. Mass loss parameters over the course of rotation experiments. Figures to the left show changes in mass fraction, M , for (a) $A_b = 1.1 \times 10^{-2} \text{ s}^2 \text{ m}^{-2}$ (80 % VCM), (c) $A_b = 9.3 \times 10^{-3} \text{ s}^2 \text{ m}^{-2}$ (50 % VCM), and (e) $A_b = 1.9 \times 10^{-3} \text{ s}^2 \text{ m}^{-2}$ (16.7 % VCM). Figures to the right show fractional mass loss per impact, Δm_* , for the same materials in (b), (d), and (f). All 5 particles of a given composition are represented on each plot, with the average ($n = 5$) depicted as a thicker black line. The number of impacts undergone by each particle have been normalized by the total number of impacts to allow comparison — mechanically strong particles in panel (a, b) underwent 4400 drops, panel (c, d) underwent 3500 drops, and mechanically weak particles in panel (e, f) underwent 25 drops. These weak particles, represented at the bottom of the figure, lost significant amounts of mass during each rotation and continued to be placed in the drum until very little of the original particle remained. Additionally, Sternberg’s law — denoted by the cyan dashed line — was fit to each plot of mass fraction. Mass fraction scales exponentially with the number of impacts in the rotating drum.

While fractional mass loss per impact generally increased and became more variable with increasing A_b (Fig. 7), data suggest that there is a range of sufficiently strong materials ($A_b < 0.1$) for which mass loss was insensitive to changes in material strength. Following Miller and Jerolmack (2020), we define an empirical mass loss parameter, $k = \Delta m / \Delta E = 2\Delta m_* / v_i^2$, and compute the average value for each material from all measured drops in the drum of all particles. Although collision energy

5 decreased through time in the experiments due to attrition, the mass loss parameter k accounts for this change in energy and thus is expected to be controlled only by material properties. Miller and Jerolmack (2020) proposed that $k = AC_1$ — i.e., that the rate of mass loss depends linearly on A_b , and confirmed that relation for their experiments in natural rocks. Our results confirm a positive correlation between k and A_b , that could be consistent with a linear relation (Fig. 8). However, data again indicate a regime of sufficiently strong materials ($A_b < 0.1$) for which mass loss is roughly constant — or, at least, is not

10 sensitive to changes in material properties.

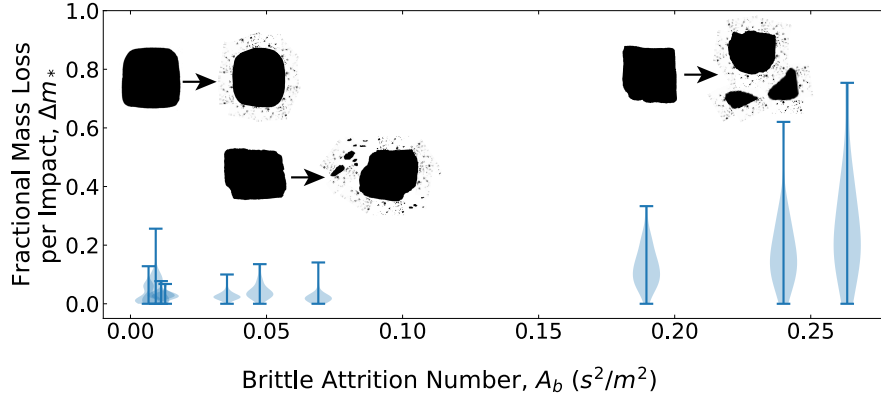


Figure 7. Violin plots illustrating the size distribution of resulting particle fragments. The fractional mass loss per impact (Δm_*) was measured for all impacts; this result is displayed as a violin plot for each material strength. Example parent and daughter particles are displayed for strong, intermediate, and weak materials to illustrate typical breakdown products after an impact or series of impacts. Mechanically weak particles (higher A_b) produced fragments in a wide range of sizes and weights, while mechanically strong particles (lower A_b) generated a narrow distribution of chip sizes. This transition occurs around $A_b = 0.1 \text{ s}^2 \text{ m}^{-2}$.

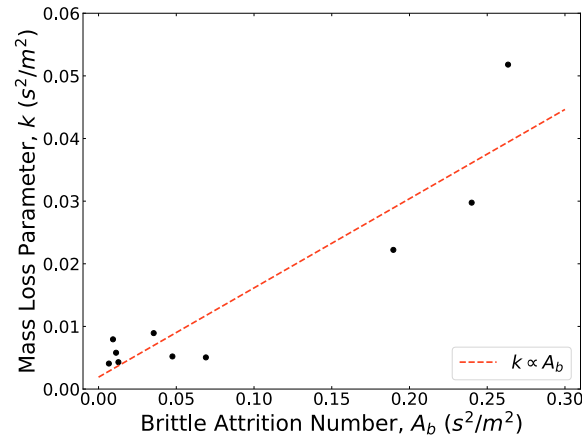


Figure 8. Relation between the empirically-determined mass loss parameter, k , and the brittle Attrition Number determined from material properties, A_b (Miller and Jerolmack, 2020); the best-fit linear relation is $k = 0.142A_b + 0.0019$, where $R^2 = 0.85$. Thus, experimental constant $C_1 = 0.14$.

3.3 Particle Shape

Particles of differing mechanical properties experienced different shape evolution trajectories. Mechanically strong particles smoothly evolved from a cuboid block toward a sphere. The mechanically weak particles began with the same cuboid shape,

	VCM [%]	σ_u [N/m ²]	Y^* [N/m ²]	ρ_s [kg/m ³]	A_b [s ² /m ²]	Number of Impacts, N_i							
						0	5	10	20	100	500	1300	3200
 Material Parameters	80	4.13e ⁶	1.11e ⁸	1.60e ³	1.13e ⁻²								
	75	3.41e ⁶	7.42e ⁷	2.13e ³	1.28e ⁻²								
	66.7	7.34e ⁶	1.63e ⁸	2.73e ³	6.64e ⁻³								
	50	2.91e ⁶	4.27e ⁷	1.73e ³	9.28e ⁻³								
	33.3	1.02e ⁶	2.15e ⁷	2.49e ³	3.55e ⁻²								
	25	6.08e ⁵	8.45e ⁶	2.36e ³	4.75e ⁻²								
	20	3.43e ⁵	6.01e ⁶	1.93e ³	6.90e ⁻²								
	16.7	1.57e ⁵	3.37e ⁶	1.74e ³	1.90e ⁻¹								
	14.3	9.72e ⁴	1.49e ⁶	1.83e ³	2.40e ⁻¹								
	12.5	1.16e ⁶	1.08e ⁷	1.99e ³	2.63e ⁻¹								

Figure 9. Progression of particle breakdown according to material parameters and approximate number of impacts; $N_i = 0$ indicates the initial shape of the particle. The material parameters of each particle type are indicated using volume concrete mix (VCM), average ultimate strength (σ_u) and modified Young's Modulus (Y^*) as measured through Instron compression tests, and average brittle Attrition Number (A_b). Also shown is particle density (ρ_s), which does not vary systematically with material strength. Mechanically strong particles achieved highly rounded shapes over thousands of rotations, while mechanically weak particles quickly fragmented into irregular shapes over 10–20 impacts. Intermediate particles exhibited both behaviors.

but fragmented into several angular pieces during their time in the rotating drum (Fig. 9). The strong particles could withstand thousands of impacts, while the weakest particles experienced 10–20 impacts before disintegrating. Particles of intermediate strength, $A_b = 6.9 \times 10^{-2} \text{ s}^2 \text{ m}^{-1}$ to $A_b = 3.6 \times 10^{-2} \text{ s}^2 \text{ m}^{-1}$ (20–33.3 % VCM) evolved from a cuboid block toward a spherical shape, but experienced several large breakage events along the trajectory toward a sphere. These intermediate particles

5 remained in the rotating drum for several hundred impacts.

Circularity, R , a measure of how closely a shape approaches a circle, increased over the course of the experiments for all materials. While the rate of change in particle shape is controlled by attrition rate, this dependence can be removed by examining particle shape as function of cumulative mass loss (μ) (Domokos et al., 2014; Szabó et al., 2015; Novák-Szabó et al., 2018). The circularity of mechanically strong particles increased smoothly and monotonically with μ toward a spherical

10 shape ($R = 1$). For intermediate and weak particles, circularity increased, but exhibited significant fluctuations associated with fragmentation events. Mechanically strong particles reached circularity values around 0.85, while weak particles reached values around 0.65 (Fig. 10). In the chipping limit associated with bed load, there is a single relation between R and μ that depends only on the initial shape of particles (Domokos et al., 2014; Szabó et al., 2015; Novák-Szabó et al., 2018; Pal et al., 2021). For

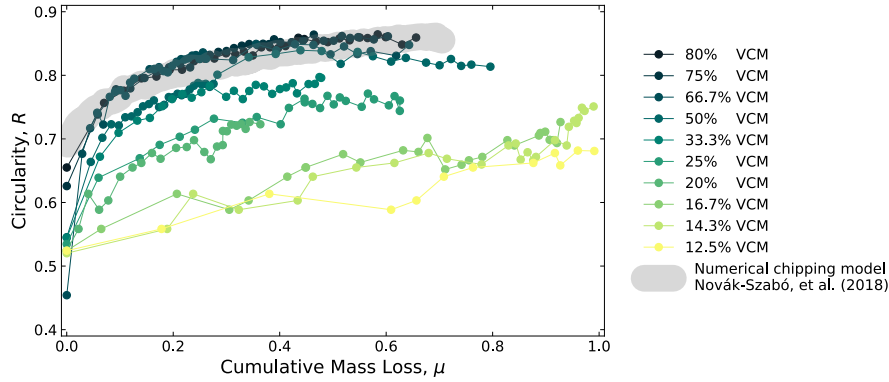


Figure 10. Circularity as a function of cumulative mass loss for all material strengths tested, where circularity measurements are averaged for all particles of a given composition ($n = 5$). Mechanically strong particles (50–80 % VCM) with $A_b \leq 0.013 \text{ s}^2 \text{ m}^{-2}$ fall within the pure chipping regime and conform to the universal curve described by Novák-Szabó et al. (2018), which is identified by the grey region.

our strong materials associated with $A_b \leq 0.013 \text{ s}^2 \text{ m}^{-2}$, we find that shape evolution is independent of material properties and closely follows the trend expected for chipping. For weaker materials, however, data exhibit a progressive departure from the expected chipping curve with increasing A_b (decreasing material strength) (Fig. 10).

4 Discussion

5 We begin this section by reminding the reader of several caveats that should be kept in mind when interpreting the experimental results. Our particles, especially the weaker ones, may not have behaved strictly as brittle materials in terms of their failure. The high proportion of sand in mechanically weak particles frequently caused fragments to disintegrate on impact, producing a large population of sand and fine concrete fragments. The population of fine fragments was not collected or measured, as this pattern of disintegration differs from fragmentation in natural rocks under comparable conditions. Weaker particles sometimes

10 exhibited complex stress-strain curves, resulting in potentially large error in estimating the material parameters required to compute A_b . Clearly, future experiments would benefit from better control in the cement preparation and testing process. Nevertheless, there are many aspects of fracture dynamics that are insensitive to the details of material properties (Oddershede et al., 1993; Ghadiri and Zhang, 2002). For example, experiments with balls of gypsum aggregate represent a canonical system for studying impact fragmentation, and are often used to benchmark numerical simulations of brittle fracture (Oddershede

15 et al., 1993; Kun and Herrmann, 1996; Åström et al., 2004). Our weak cements behave similarly to gypsum aggregates and weak sandstones, while the strongest cement mixtures are comparable to limestone. Furthermore, although direct comparisons cannot be drawn, our measured values for the ultimate strength of concrete particles are comparable to the tensile strength values of natural and artificial materials determined by Sklar and Dietrich (2001).

The most important result from our study is the first experimental confirmation of a continuous phase transition from chipping to fragmentation. Ghadiri and Zhang (2002) proposed that in the low energy limit of impact attrition, the number of impacts required to cause dynamic fragmentation, N_i , diverges. This defines the chipping limit, where fatigue failure and whole particle breakage does not occur; attrition is accomplished only by the formation of shallow compressional cracks at the contact zone. As collision energy increases, they proposed that N_i drops continuously toward a dynamic fragmentation limit associated with $N_i = 1$ (Ghadiri and Zhang, 2002). To compare our findings to their conceptual model, we must assume an equivalence between impact energy and material strength. Such an equivalence is implicit in the generic attrition model (Eq. 1). We acknowledge that defining a ‘fragmentation’ event is arbitrary, as it requires assigning a threshold fragment size or fractional mass loss that is sufficiently large to be considered a fragment (and not a ‘chip’). Regardless of the chosen threshold, however, our results show the expected continuous transition from chipping to fragmentation (Fig. 11). Moreover, this agreement supports the notion that changes in material strength are dynamically equivalent to changes in impact energy, and that the former may be characterized with A_b .

Experimental results also support the recent numerical simulations of Pal et al. (2021), that map the attrition mechanisms of chipping and fragmentation to distinct patterns of mass loss and shape evolution. The chipping limit is defined by (i) a small fractional mass loss (Figs. 7; 8) and (ii) the smooth evolution of particle shape toward a sphere (Fig. 10), both of which depend only weakly on material strength (or collision energy). In other words, experiments and simulations characterize the parameter space where pure chipping lives; here, mass loss follows Sternberg’s law and shape evolution follows a universal rounding that is purely geometric (Novák-Szabó et al., 2018). The transition to fatigue failure (or ‘cleavage’, cf. Pal et al. (2021)) occurs at a critical value for A_b (or collision energy), beyond which mass loss rapidly increases with decreasing material strength (or increasing collision energy) (Figs. 7; 8). In this fatigue failure regime, mass loss and shape evolution trends become more erratic, and progressively depart from Sternberg’s law and universal rounding, respectively, with decreasing material strength (increasing collision energy). Pal et al. (2021) noted that the cleavage regime of impact attrition in their simulations followed the Basquin law of subcritical failure: material failure occurs at a finite timescale, which decreases as a power-law function of the stress amplitude. Translating this law to our experiments, we would predict that the critical number of collisions required to fragment a particle, N_i , increases as a power law with increasing material strength (decreasing A_b). While we are cautious in drawing quantitative conclusions from our data given the noise and limitations described above, our results are qualitatively consistent with the Basquin law (Fig. 11).

Our results suggest a bi-partite relation between A_b and attrition mass loss (Fig. 8), which differs from the linear relation between A_b and k that was suggested by the experiments of Miller and Jerolmack (2020). While this difference may be the result of variation and/or error in our measurements — and we cannot directly compare values for A_b since material properties were measured using different techniques — we note that the range of A_b explored in this study is roughly three times larger than that of Miller and Jerolmack (2020). In addition, the mass loss rates in the Miller and Jerolmack (2020) study were much lower than here, due to both stronger materials and smaller collision energies. The simplest explanation is that there are two distinct mass loss regimes corresponding to the two distinct attrition mechanisms, as seen in the simulations of Pal et al. (2021). The well-controlled Miller and Jerolmack (2020) experiment, with stronger particles at lower energies, probed only

the chipping regime. We speculate that the large variation in our material parameter measurements obscures the more subtle trend of k and A_b that is expected in the chipping regime; instead, only the rapid nonlinear increase of mass loss in the fatigue failure regime is resolved in our data (Fig. 8).

It is natural for the reader to wonder if and how our findings may be applied to the field, either directly by some appropriate scaling or indirectly through a numerical model. Collisions of particles with each other and the bed are more complicated in nature than our simplified experiments, and will vary among environments (bed load, debris flow, or rock fall). Miller and Jerolmack (2020) outline some of the differences between single-impact and bed-normal collisions in experiments such as ours, and the multi-body and tangential collisions that occur for the specific case of bed load. Quite simply, attrition rates measured from drop experiments cannot and should not be scaled directly to the field. The utility of our experiments, instead, lies in testing the fundamentals of impact attrition and dynamic fracture, which is an essential component of models for pebble and bedrock erosion. Our findings, which corroborate numerical simulations (Pal et al., 2021), point to the importance in distinguishing attrition mechanisms when modeling collision-driven erosion. “Saltation abrasion” models for bedrock incision typically encode some version of Eq. 1, and are most appropriate for the chipping regime — although our results here and in Miller and Jerolmack (2020) indicate that A_b should be determined, rather than simply using tensile strength as is commonly done (Sklar and Dietrich, 2004; Lamb et al., 2015). Determining the threshold energy and material strength associated with the transition from chipping to fatigue failure, for materials of interest in natural settings, becomes of critical importance for selecting an attrition relation. We recommend that future work begin with a more controlled experimental approach: using a wide range of natural rock materials, more stringent material property measurements, a wide range of collision energies, and a full analysis of attrition product sizes and shapes. In this manner, the universal phase transition from chipping to fragmentation that was proposed by Pal et al. (2021) could be quantitatively vetted for geologic materials, and across the entire ranges of energy and material strength that are relevant for geophysical flows. Given the universality of pebble mass and shape evolution in the chipping regime (Novák-Szabó et al., 2018; Miller and Jerolmack, 2020), the Basquin law for fatigue failure in the cleavage regime (Pal et al., 2021), and the generic nature of fragmentation (Domokos et al., 2015, 2020), we are reasonably confident that future experiments will confirm and extend our findings.

25 5 Conclusions

This study connected attrition mechanism to the resulting shape evolution and mass loss of concrete particles in order to better understand the transition from chipping to fragmentation. By simulating transport over a wide range of material strengths, we were able to populate a phase space for attrition. Concrete particles were rotated in a metal drum to simulate transport, and results indicate that mechanically strong particles evolved smoothly and monotonically toward a spherical shape, while weak particles rapidly broke apart into irregular, angular pieces. Particles of intermediate strength experienced fatigue failure, and erratically evolved toward a more rounded shape.

For suitably strong materials, particle shape evolution followed a single curve that was independent of material properties, and mass loss followed the exponential Sternberg’s law. This is the pure chipping limit of impact attrition. This condition ap-

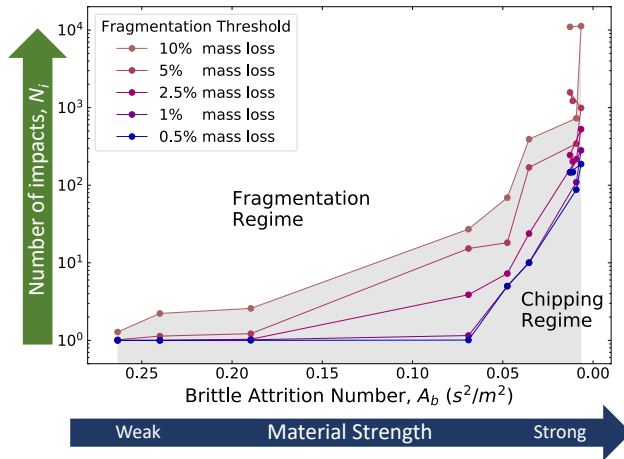


Figure 11. Experimentally determined phase space for attrition showing the approximate number of impacts required to fragment particles of different material strength. The fragmentation threshold, or boundary between the chipping and fragmentation regimes, is defined by the fraction of mass lost during a given impact (e.g., fragmentation occurs if 10 % of a particle’s current mass is lost).

appears to be common, even universal, for natural rocks undergoing bed-load transport (Novák-Szabó et al., 2018). The agreement of our experiments using concrete blocks, with previously described universal rounding, affirms the robustness of geometric shape evolution by chipping and also the relevance of our experiments to natural pebbles. As material strength decreased in our experiments beyond a threshold value for A_b , shape evolution and mass loss became more erratic and deviated from the chipping trends. This fatigue failure regime can be thought of as representing a continuous phase transition from pure chipping to pure fragmentation, where the number of collisions required to break a particle decreases as material strength weakens. This picture is consistent with the probabilistic conceptual model of Zhang and Ghadiri (2002) and recent numerical simulations of Pal et al. (2021), where this transition was cast as a function of impact energy. Sufficiently weak materials (or large collision energies) will catastrophically fail with a single impact; this limit is likely reached in nature for rockfalls and landslides. This work suggests that the parameter grouping $A_b \Delta E$ may serve to predict the attrition regime, which would allow one to constrain the energy associated with sediment transport from particle shape in the field (Novák-Szabó et al., 2018).

The transition from chipping to fatigue failure marks the limit of applicability for the geometric model of pebble rounding (Novák-Szabó et al., 2018). This is important because, in the chipping limit, this model may be used to infer the transport distance of river pebbles from their shape (Szabó et al., 2015; Novák-Szabó et al., 2018). The chipping-fragmentation threshold is also important for models of bedrock erosion by bed-load transport (“saltation abrasion”), as they implicitly assume that there is only one regime of impact attrition (Sklar and Dietrich, 2004; Lamb et al., 2015). These models may be most appropriate for the chipping regime, yet cannot predict the onset of fatigue failure or the rapid increase in mass loss associated with it. While we urge caution in applying saltation erosion models until the thresholds for fatigue failure of relevant materials are determined, the morphology of bedrock channel beds may provide helpful qualitative information. In particular, the chipping

regime of bed-load erosion should produce bedrock channel morphologies that are smooth down to the scale of impactors (Sipos et al., 2011), while fatigue failure would drive fragmentation of the channel and create rough and angular features.

Data availability. All relevant data used to generate the figures in this paper are deposited in figshare, a free and open repository. These datasets can be accessed using the following link: <https://doi.org/10.6084/m9.figshare.14069105>.

5 *Author contributions.* S.B. conducted the experiments, led data analysis, and wrote the paper. D.J.J. supervised the research, assisted in analysis and interpretation of data, and edited the paper.

Competing interests. The authors declare that they have no conflict of interest.

Disclaimer. The authors declare no conflicts of interest.

10 *Acknowledgements.* This work was supported by the University of Pennsylvania Center for Undergraduate Research Fellowships, and the Hayden Scholars program of the Department of Earth and Environmental Science. We thank Kimberly Miller for supplying images, and for helpful discussions.

References

- Adams, J.: Wear of unsound pebbles in river headwaters, *Science*, 203, 171–172, 1979.
- Anderson, R. S.: Erosion profiles due to particles entrained by wind: Application of an eolian sediment-transport model, *Geological Society of America Bulletin*, 97, 1270–1278, 1986.
- 5 Arabnia, O. and Sklar, L. S.: Experimental study of particle size reduction in geophysical granular flows, *Int. J. Erosion Control Eng.*, 9, 122–129, 2016.
- Åström, J., Linna, R., Timonen, J., Møller, P. F., and Oddershede, L.: Exponential and power-law mass distributions in brittle fragmentation, *Physical Review E*, 70, 026 104, 2004.
- Attal, M. and Lavé, J.: Pebble abrasion during fluvial transport: Experimental results and implications for the evolution of the sediment along
10 rivers, *J. Geophys. Res.*, 114, F04 023, <https://doi.org/10.1029/2009JF001328>, 2009.
- Bemrose, C. R. and Bridgwater, J.: A review of attrition and attrition test methods, *Powder Tech.*, 49, 97–126, 1987.
- Bernd, I., Laue, J., and Springman, S. M.: Fractal fragmentation of rocks within sturzstroms: insight derived from physical experiments within the ETH geotechnical drum centrifuge, *Granular Matter*, 12, 267–285, <https://doi.org/10.1007/s10035-009-0163-1>, 2010.
- Beschta, R. L.: Channel changes following storm-induced hillslope erosion in the Upper Kowai Basin, Torlesse Range, New Zealand, *Journal
15 of Hydrology (New Zealand)*, pp. 93–111, 1983.
- Bitter, J. G. A.: A study of erosion phenomena, part I, *Wear*, 6, 5–21, [https://doi.org/10.1016/0043-1648\(63\)90003-6](https://doi.org/10.1016/0043-1648(63)90003-6), 1963.
- Chapman, R. W. and Greenfield, M. A.: Spheroidal weathering of igneous rocks, *American Journal of Science*, 247, 407–429, 1949.
- Domokos, G., Sipos, A., Szabó, G. M., and Várkonyi, P. L.: Formation of sharp edges and planar areas of asteroids by polyhedral abrasion, *Astrophys. J.*, 699, L13–L16, <https://doi.org/10.1088/0004-637X/699/1/L13>, 2009.
- 20 Domokos, G., Jerolmack, D. J., Sipos, A., and Török, J.: How river rocks round: resolving the shape size paradox, *PLoS One*, 9, e88 657, <https://doi.org/10.1371/journal.pone.0088657>, 2014.
- Domokos, G., Kun, F., Sipos, A., and Szabó, T.: Universality of fragment shapes, *Sci. Rep.*, 5, 9147, <https://doi.org/10.1038/srep09147>, 2015.
- Domokos, G., Jerolmack, D. J., Kun, F., and Török, J.: Plato's cube and the natural geometry of fragmentation, *Proceedings of the National
25 Academy of Sciences*, 117, 18 178–18 185, 2020.
- Engle, P. A.: *Impact Wear of Materials*, Elsevier, Sci., New York, 1978.
- Firey, W. J.: Shapes of worn stones, *Mathematika*, 21, 1–11, <https://doi.org/10.1112/S0025579300005714>, 1974.
- Ghadiri, M. and Zhang, Z.: Impact attrition of particulate solids. Part 1: A theoretical model of chipping, *Chem. Eng. Sci.*, 57, 3659–3669, 2002.
- 30 Grady, D. E.: Length scales and size distributions in dynamic fragmentation, *Int. J. Fracture*, 163, 85–99, <https://doi.org/10.1007/s10704-009-9418-4>, 2010.
- Greeley, R. and Iversen, J. D.: *Wind as a geological process: on Earth, Mars, Venus and Titan*, vol. 4, CUP Archive, 1987.
- Hovius, N., Stark, C. P., and Allen, P. A.: Sediment flux from a mountain belt derived by landslide mapping, *Geology*, 25, 231–234, 1997.
- Hovius, N., Stark, C. P., Hao-Tsu, C., and Jiun-Chuan, L.: Supply and removal of sediment in a landslide-dominated mountain belt: Central
35 Range, Taiwan, *The Journal of Geology*, 108, 73–89, 2000.
- Jerolmack, D. J. and Brzinski, T. A.: Equivalence of abrupt grain-size transitions in alluvial rivers and eolian sand seas: A hypothesis, *Geology*, 38, 716–722, <https://doi.org/10.1130/G30922.1>, 2010.

- Johnson, J. P. and Whipple, K. X.: Feedbacks between erosion and sediment transport in experimental bedrock channels, *Earth Surface Processes and Landforms*, 32, 1048–1062, <https://doi.org/10.1002/esp.1471>, 2007.
- Kodama, Y.: Experimental study of abrasion and its role in producing downstream fining in gravel-bed rivers, *J. Sediment Res.*, A64, 76–85, 1994.
- 5 Krumbein, W. C.: Measurement and geological significance of shape and roundness of sedimentary particles, *J. Sediment Petrol.*, 11, 64–72, 1941.
- Kuenen, P. H.: Experimental abrasion of pebbles: rolling by current, *J. Geol.*, 64, 336–368, 1956.
- Kun, F. and Herrmann, H. J.: A study of fragmentation processes using a discrete element method, *Computer Methods in Applied Mechanics and Engineering*, 138, 3–18, 1996.
- 10 Kun, F. and Herrmann, H. J.: Transition from damage to fragmentation in collision of solids, *Phys. Rev. E*, 59, 2623, <https://doi.org/10.1103/PhysRevE.59.2623>, 1999.
- Lamb, M. P., Finnegan, N. J., Scheingross, J. S., and Sklar, L. S.: New insights into the mechanics of fluvial bedrock erosion through flume experiments and theory, *Geomorphology*, 244, 33–55, 2015.
- Lan, H., Martin, C. D., and Hu, B.: Effect of heterogeneity of brittle rock on micromechanical extensile behavior during compression and
15 loading, *J. Geophys. Res.*, 115, B01 202, <https://doi.org/10.1029/2009JB006496>, 2010.
- Lewin, J. and Brewer, P. A.: Laboratory simulation of clast abrasion, *Earth. Surf. Process. Landf.*, 27, 145–164, <https://doi.org/10.1002/esp.306>, 2002.
- Miller, K. L. and Jerolmack, D.: Controls on the rates and products of particle attrition by bed-load collisions, *Earth Surface Dynamics Discussions*, 2020, 1–29, <https://doi.org/10.5194/esurf-2020-86>, 2020.
- 20 Miller, K. L., Szabó, T., Jerolmack, D. J., and Domokos, G.: Quantifying the significance of abrasion and size selective transport for downstream fluvial grain size evolution, *J. Geophys. Res.-Earth*, 119, 2412–2429, <https://doi.org/10.1002/2014JF003156>, 2014.
- Mohajerani, A. and Spelt, J.: Edge chipping of borosilicate glass by blunt indentation, *Mechanics of materials*, 42, 1064–1080, 2010.
- Moss, A. J., Walker, P. H., and Hutka, J.: Fragmentation of granitic quartz in water, *Sedimentology*, 20, 489–511, <https://doi.org/10.1111/j.1365-3091.1973.tb01627.x>, 1973.
- 25 Novák-Szabó, T., Sipos, A. , Shaw, S., Bertoni, D., Pozzebon, A., Grotolli, E., Sarti, G., Ciavola, P., Domokos, G., and Jerolmack, D. J.: Universal characteristics of particle shape evolution by bed-load chipping, *Sci. Adv.*, 4, eaao4946, <https://doi.org/10.1126/sciadv.aao4946>, 2018.
- Oddershede, L., Dimon, P., and Bohr, J.: Self-organized criticality in fragmenting, *Physical review letters*, 71, 3107, 1993.
- Okumura, S.: Weathering process of Nabari gabbroic body (1) Zoning of weathering crust, *The Journal of the Japanese Association of
30 Mineralogists, Petrologists and Economic Geologists*, 77, 191–202, 1982.
- Ollier, C.: Spheroidal weathering, exfoliation and constant volume alteration, *Zeitschrift fur Gromorphologie*, 11, 103–108, 1967.
- Pal, G., Domokos, G., and Kun, F.: How curvature flows: scaling laws and global geometry of impact induced attrition processes, *arXiv preprint arXiv:2105.12198*, 2021.
- Perfect, E.: Fractal models for the fragmentation of rocks and soils: a review, *Eng. Geology*, 48, 185–198, [https://doi.org/10.1016/S0013-7952\(97\)00040-9](https://doi.org/10.1016/S0013-7952(97)00040-9), 1997.
- 35 Perras, M. A. and Diederichs, M. S.: A review of the tensile strength of rock: concepts and testing, *Geotechnical and geological engineering*, 32, 525–546, 2014.

- Rhee, Y.-W., Kim, H.-W., Deng, Y., and Lawn, B. R.: Brittle fracture versus quasi plasticity in ceramics: a simple predictive index, *Journal of the American Ceramic Society*, 84, 561–565, 2001.
- Rogers, J. J. W. and Schubert, C.: Size distributions of sedimentary populations, *Science*, 141, 801–802, <https://doi.org/10.1126/science.141.3583.801>, 1963.
- 5 Sak, P. B., Navarre-Sitchler, A. K., Miller, C. E., Daniel, C. C., Gaillardet, J., Buss, H. L., Lebedeva, M. I., and Brantley, S. L.: Controls on rind thickness on basaltic andesite clasts weathering in Guadeloupe, *Chemical Geology*, 276, 129–143, 2010.
- Salman, A., Reynolds, G., Fu, J., Cheong, Y., Biggs, C., Adams, M., Gorham, D., Lukenics, J., and Hounslow, M.: Descriptive classification of the impact failure modes of spherical particles, *Powder Technology*, 143, 19–30, 2004a.
- Salman, A. D., Reynolds, G. K., Fu, J. S., Cheong, Y. S., Biggs, C. A., Adams, M. J., Gorham, D. A., Lukenics, J., and Hounslow, M. J.: Descriptive classification of the impact failure modes of spherical particles, *Powder Technol.*, 143–144, 19–30, 10 <https://doi.org/10.1016/j.powtec.2004.04.005>, 2004b.
- Simpson, D. R.: Exfoliation in the Upper Pocahontas Sandstone, Mercer County, West Virginia, *American Journal of Science*, 262, 545–551, 1964.
- Sipos, A. A., Domokos, G., Wilson, A., and Hovius, N.: A discrete random model describing bedrock profile abrasion, *Mathematical Geosciences*, 43, 583–591, 2011.
- 15 Sklar, L. S. and Dietrich, W. E.: Sediment and rick strength controls on river incision into bedrock, *Geology*, 29, 1087–1090, [https://doi.org/10.1130/0091-7613\(2001\)029<1087:SARSCO>2.0.CO;2](https://doi.org/10.1130/0091-7613(2001)029<1087:SARSCO>2.0.CO;2), 2001.
- Sklar, L. S. and Dietrich, W. E.: A mechanistic model for river incision into bedrock by saltating bed load, *Water Resour. Res.*, 40, W06 301, <https://doi.org/10.1029/2003WR002496>, 2004.
- 20 Sternberg, H.: Untersuchungen über längen-und Querprofil Geschiebef Ührender Flüsse, *Zeitschrift für Bauwesen*, 25, 486–506, 1875.
- Szabó, T., Fityus, S., and Domokos, G.: Abrasion model of downstream changes in grain shape and size along the Williams River, Australia, *J. Geophys. Res.-Earth*, 118, 2059–2071, <https://doi.org/10.1002/jgrf.20142>, 2013.
- Szabó, T., Domokos, G., Grotzinger, J. P., and Jerolmack, D. J.: Reconstructing the transport history of pebbles on Mars, *Nat. Commun.*, 6, 8366, <https://doi.org/10.1038/ncomms9366>, 2015.
- 25 Tavares, L. M. and das Neves, P. B.: Microstructure of quarry rocks and relationships to particle breakage and crushing, *Int. J. Mineral Process.*, 87, 28–41, <https://doi.org/10.1016/j.minpro.2008.01.007>, 2008.
- Tavares, L. M. and King, R. P.: Single-particle fracture under impact loading, *Int. J. Mineral Process.*, 54, 1–28, [https://doi.org/10.1016/S0301-7516\(98\)00005-2](https://doi.org/10.1016/S0301-7516(98)00005-2), 1998.
- van Steijn, H.: Debris-flow magnitude—frequency relationships for mountainous regions of Central and Northwest Europe, *Geomorphology*, 30 15, 259–273, 1996.
- Vasconcelos, G. and Lourenço, P. B.: Experimental characterization of stone masonry in shear and compression, *Construction and Building Materials*, 23, 3337–3345, <https://doi.org/10.1016/j.conbuildmat.2009.06.045>, 2009.
- Várkonyi, P. L. and Domokos, G.: A general model for collision-based abrasion processes, *IMA J. Appl. Math.*, 76, 47–56, <https://doi.org/10.1093/imamat/hxq066>, 2011.
- 35 Wang, X.-e., Yang, J., Liu, Q.-f., Zhang, Y.-m., and Zhao, C.: A comparative study of numerical modelling techniques for the fracture of brittle materials with specific reference to glass, *Engineering Structures*, 152, 493–505, 2017.
- Wang, Z.-T., Wang, H.-T., Niu, Q.-H., Dong, Z.-B., and Wang, T.: Abrasion of yardangs, *Phys. Rev. E*, 84, 031 304, <https://doi.org/10.1103/PhysRevE.84.031304>, 2011.

Wilshaw, T.: The Hertzian fracture test, *Journal of Physics D: Applied Physics*, 4, 1567, 1971.

Yashima, S., Kanda, Y., and Sano, S.: Relationships between particle size and fracture energy or impact velocity required to fracture as estimated from single particle crushing, *Powder Tech.*, 51, 277–282, [https://doi.org/10.1016/0032-5910\(87\)80030-X](https://doi.org/10.1016/0032-5910(87)80030-X), 1987.

Zhang, Z. and Ghadiri, M.: Impact attrition of particulate solids. Part 2: Experimental work, *Chem. Eng. Sci.*, 57, 3671–3686, 2002.